



## Submesoscale Water-Mass Spectra in the Sargasso Sea

E. KUNZE,\* J. M. KLYMAK,<sup>+</sup> R.-C. LIEN,<sup>#</sup> R. FERRARI,<sup>@</sup> C. M. LEE,<sup>#</sup>  
M. A. SUNDERMEYER,<sup>&</sup> AND L. GOODMAN<sup>&</sup>

<sup>\*</sup> *NorthWest Research Associates, Redmond, Washington*

<sup>+</sup> *University of Victoria, Victoria, British Columbia, Canada*

<sup>#</sup> *Applied Physics Lab, University of Washington, Seattle, Washington*

<sup>@</sup> *Massachusetts Institute of Technology, Cambridge, Massachusetts*

<sup>&</sup> *University of Massachusetts Dartmouth, New Bedford, Massachusetts*

(Manuscript received 10 June 2014, in final form 20 February 2015)

### ABSTRACT

Submesoscale stirring contributes to the cascade of tracer variance from large to small scales. Multiple nested surveys in the summer Sargasso Sea with tow-yo and autonomous platforms captured submesoscale water-mass variability in the seasonal pycnocline at 20–60-m depths. To filter out internal waves that dominate dynamic signals on these scales, spectra for salinity anomalies on isopycnals were formed. Salinity-gradient spectra are approximately flat with slopes of  $-0.2 \pm 0.2$  over horizontal wavelengths of 0.03–10 km. While the two to three realizations presented here might be biased, more representative measurements in the literature are consistent with a nearly flat submesoscale passive tracer gradient spectrum for horizontal wavelengths in excess of 1 km. A review of mechanisms that could be responsible for a flat passive tracer gradient spectrum rules out (i) quasigeostrophic eddy stirring, (ii) atmospheric forcing through a relict submesoscale winter mixed layer structure or nocturnal mixed layer deepening, (iii) a downscale vortical-mode cascade, and (iv) horizontal diffusion because of shear dispersion of diapycnal mixing. Internal-wave horizontal strain appears to be able to explain horizontal wavenumbers of 0.1–7 cycles per kilometer (cpkm) but not the highest resolved wavenumbers (7–30 cpkm). Submesoscale subduction cannot be ruled out at these depths, though previous observations observe a flat spectrum well below subduction depths, so this seems unlikely. Primitive equation numerical modeling suggests that nonquasigeostrophic subinertial horizontal stirring can produce a flat spectrum. The last need not be limited to mode-one interior or surface Rossby wavenumbers of quasigeostrophic theory but may have a broadband spectrum extending to smaller horizontal scales associated with frontogenesis and frontal instabilities as well as internal waves.

### 1. Introduction

Submesoscale stirring facilitates the cascade of water-mass and other tracer variances from  $O(100)$  km scales associated with the mesoscale eddy field to small scales and eventual eradication by molecular mixing (Stern 1975). Finescale temperature anomalies  $T'$  will also influence acoustic propagation. Passive tracers such as water-mass anomalies on isopycnals are not dynamically constrained by any length scale or balance considerations, and so will eventually cascade to isotropic turbulence and molecular diffusivity scales (Stern 1975; Ferrari and Polzin 2005). While quasigeostrophic (QG)

turbulence theory, observations, and numerical modeling have advanced our understanding of subinertial mesoscale physics (Charney 1971; Smith et al. 2002; Smith and Ferrari 2009), submesoscale dynamics pose a modeling challenge because quasigeostrophic assumptions break down (Boccaletti et al. 2007; Klein et al. 2008; Molemaker et al. 2010; Capet et al. 2008a,b; Tulloch et al. 2011) and an observational challenge because internal gravity waves dominate dynamic [horizontal kinetic energy (HKE) and available potential (APE)] signals, leaving only tracers as possible signatures of subinertial submesoscale dynamics. Early attempts to isolate the submesoscale subinertial variability from internal waves observationally using potential vorticity (PV) and other consistency relations were frustrated by demands on time–space sampling (Müller et al. 1988; Kunze and Sanford 1993; Kunze 1993; Polzin et al. 2003).

Corresponding author address: E. Kunze, NorthWest Research Associates, 4126 148th Ave., Redmond, WA 98052.  
E-mail: ericleekunze@gmail.com

On dimensional grounds, turbulence theory (Batchelor 1959) suggests that, on length scales smaller than those of the dominant shear, that is, on length scales where only shear from larger scales stirs, the passive tracer gradient spectrum should behave as  $k^1$ , where  $k$  is the wavenumber. For a quasigeostrophic eddy field, the length scale that dominates shear is the Rossby radius of deformation  $NH/f$  or larger, where  $N$  is the buoyancy frequency,  $H$  is a vertical length scale, and  $f$  is the Coriolis frequency. For the midlatitude open ocean, the Rossby mode-one radius of deformation is  $O(100)$  km. Thus, the submesoscale, defined here as length scales smaller than the Rossby deformation radius, should have a  $k^1$  passive tracer gradient spectrum according to quasigeostrophic theory (Charney 1971) and as confirmed by quasigeostrophic numerical simulations of mesoscale stirring (Smith and Ferrari 2009). Any additional shearing from smaller, that is, submesoscale, length scales will increase the cascade rate to high wavenumbers and hence redden (i.e., produce a more negative slope in) the passive tracer spectrum. Near boundaries like the surface, quasigeostrophic dynamics predict frontogenesis and a flatter energy spectrum; this regime is referred to as surface quasigeostrophy (SQG). In SQG, the Rossby deformation length scale is  $\int N(z) dz/f$ , decreasing toward the surface (Scott 2006) with a  $k^{1/3}$  passive tracer gradient spectrum at larger scales and again a  $k^1$  Batchelor spectrum at smaller scales.

Observations spanning length scales  $O(1\text{--}100)$  km most often report water-mass spectra along isopycnals with redder (more negative) slopes than the quasigeostrophic prediction of  $k^1$  (Ferrari and Rudnick 2000; Cole et al. 2010; Cole and Rudnick 2012; Klymak et al. 2015; Callies and Ferrari 2013). Moreover, according to surface quasigeostrophic theory (Scott 2006), spectral slopes in the submesoscale band should become bluer (more positive slope) with depth in the upper ocean, whereas observations find them becoming redder (Klymak et al. 2015; Callies and Ferrari 2013). Primitive equation numerical simulations reproduce the observed  $k^0$  gradient spectrum in the submesoscale band (Capet et al. 2008a; Klein et al. 2008), albeit at fixed depths not isopycnals, making them hard to interpret, while quasigeostrophic models do not (Smith and Ferrari 2009). Nevertheless, the primitive equation simulations support the notion that nonquasigeostrophic dynamics are responsible for the observed slopes.

Section 2 describes the background environment, section 3 defines instrumentation and measurements, section 4 discusses spectral analysis methods, section 5 relates our horizontal wavenumber spectrum for salinity gradients on isopycnals, section 6 defines previous similar measurements, section 7 discusses possible explanations for the observed spectral slopes, and section 8 offers conclusions.

## 2. Background environment

As part of the Office of Naval Research's Lateral Mixing Directed Research Initiative (LatMix) June 2011 field program, two Sargasso Sea sites near  $32^\circ\text{N}$ ,  $73^\circ\text{W}$  (Coriolis frequency  $f = 7.7 \times 10^{-5} \text{ rad s}^{-1}$ ) with different eddy confluences were sampled around two rhodamine dye injections (Shcherbina et al. 2015); confluence (equivalently, rate of strain, rate of deformation, or straining) is defined as  $[(u_x - v_y)^2 + (v_x + u_y)^2]^{1/2}$  and is the time derivative of strain or deformation. At both sites, the mixed layer depth was  $\sim 10$  m but reached  $\sim 30$  m during the nights of 15 and 19 June at site 2. Stratification in the seasonal upper pycnocline immediately below the mixed layer base was  $N \sim 10^{-2} \text{ rad s}^{-1}$ .

Site 1 was sampled during 2–10 June 2011. It was characterized by a very weak eddy field with 1–10-km drifter array–based confluences less than  $10^{-6} \text{ s}^{-1} \sim 0.01f$  (D. A. Birch et al. 2014, unpublished manuscript), that is, 1–5-km Rossby numbers  $O(0.01)$ , little water-mass variability (rms isopycnal salinity anomalies  $S'$  of  $0.036 \text{ g kg}^{-1}$ ) at the dye injection site, and internal-wave spectral levels at roughly half canonical levels (Shcherbina et al. 2015; Munk 1981). Isopycnal salinity anomalies  $S'$  and vertical displacements  $\xi$  relative to survey means were uncorrelated, consistent with the expectation that internal waves dominate vertical displacements but do not affect salinity anomalies on density surfaces (though this need not be the case in the presence of isopycnal salinity gradients subject to internal-wave straining, as we shall see).

Site 2 was sampled during 10–19 June 2011. Confluences based on a 1–10-km drifter array were  $\sim 3 \times 10^{-5} \text{ s}^{-1} \sim 0.38f$  on 13 June, reducing to  $\sim 10^{-6} \text{ s}^{-1} \sim 0.01f$  during 14–18 June (D. A. Birch et al. 2014, unpublished manuscript), which sharpened a meridional water-mass front (Figs. 1–3) and accelerated a north-northwestward jet that subsequently relaxed between 18 and 19 June. RMS isopycnal salinity anomalies ( $0.08 \text{ g kg}^{-1}$ ) and vertical displacements (2–4 m) were partially correlated, suggesting the presence of subinertial advective, as well as internal-wave, contributions to the variability. The site 2 internal-wave energy was near canonical levels (Shcherbina et al. 2015).

## 3. Instruments and measurements

An unprecedented number of tow-yo and autonomous bodies surveyed the upper 60–150 m of the pycnocline in the vicinity of sites 1 and 2 rhodamine injections to characterize meso- to submesoscale variability (Shcherbina et al. 2015). These measurements spanned  $31^\circ 30' \text{--} 34^\circ 30' \text{N}$ ,  $72^\circ 30' \text{--} 74^\circ 30' \text{W}$ .

Here, we report on a synthesis of data from five measurement platforms that conducted multiple nested

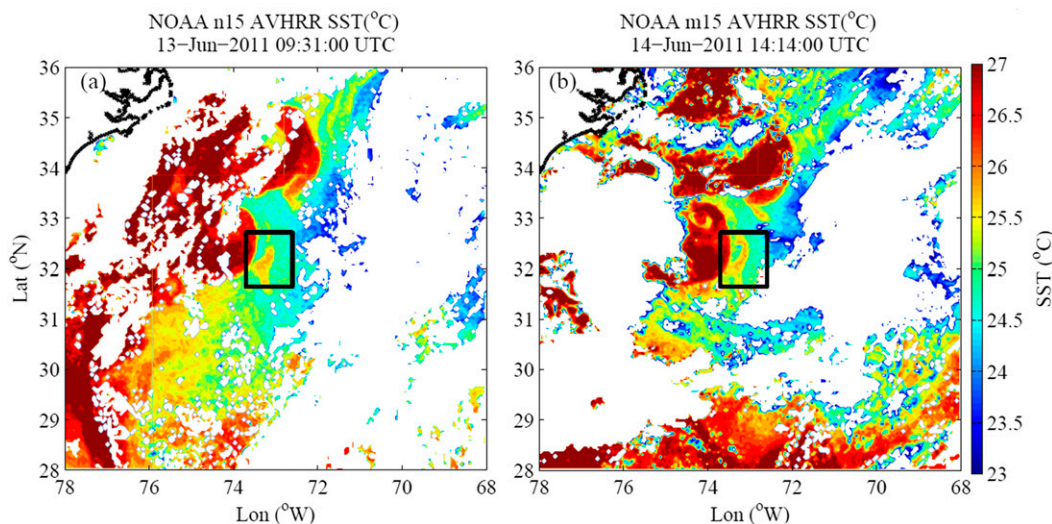


FIG. 1. Evolution of AVHRR SST between 13 and 14 Jun 2011 at the onset of the site 2 occupation (black boxes) of the eastern side of a weak warm intrusion to the east of a warmer feature. The sampled feature is elongating meridionally and sharpening zonally.

surveys (Fig. 4) to span the horizontal length scales from the meso- to the finescale (Shcherbina et al. 2015). All but one of the platforms measured temperature, salinity, and pressure with Seabird sensors. The Triaxus body was towed at 7–8 knots (kt;  $1 \text{ kt} = 0.51 \text{ m s}^{-1}$ ) while undulating between the surface and 100-m depth. Triaxus conducted 35-km radiator surveys with a horizontal resolution of  $\sim 0.5 \text{ km}$  to capture the meso- to submesoscale range. The Moving Vessel Profiler's (MVP) freefall sensor platform was dropped to a depth of 50–200 m, while being towed at 6–8 kt; the horizontal spacing for 100-m deep profiles at 7 kt is 0.55 km. MVP carried out repeated, 15-km, cross-shaped butterfly surveys to follow the time evolution of submesoscale fields. This revealed the sharpening of a meridional water-mass front between isopycnal-averaged depths of 30–70 m during 12–15 June (Fig. 3). The sharpening was not monotonic but oscillated because of periodic tilting by near-inertial shear. On eight occasions, platform Hammerhead tow-yoed in 2-km radius circles around 1-km box surveys by the Turbulent-Remote Environmental Monitoring Units (T-REMUS) autonomous underwater vehicle (AUV) that undulated between 25- and 45-m depth for 5–9 h. Both platforms circled a Gateway buoy drogued to the dye injection depth (Shcherbina et al. 2015) in order to stay in a roughly Lagrangian frame. Hammerhead was tow-yoed within  $\pm 5 \text{ m}$  of the target dye injection density (Fig. 5), spanning  $z = 15\text{--}60\text{-m}$  depth ( $\sigma_\theta = 24.6\text{--}25.7 \text{ kg m}^{-3}$ ) depending on the survey, in an effort to resolve the smallest possible horizontal scales. Horizontal separations at midvertical aperture for both Hammerhead and

T-REMUS are about 100 m but approach zero near the apex and zeniths of their vertical excursion. Since both platforms undulated in the upper pycnocline, all their data were used, including horizontal separations  $O(10) \text{ m}$  near the tops and bottoms of their vertical trajectories (Fig. 5). Occasional encounters with rhodamine and

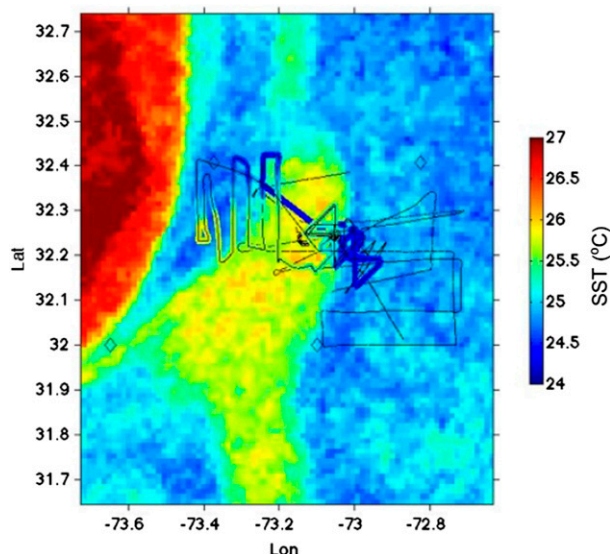


FIG. 2. Close-up of site 2 sampling in the warm filament (black boxes in Fig. 1), showing the radiator pattern Triaxus and butterfly pattern MVP tow-yo surveys superimposed on AVHRR SST from 13 Jun 2011. The black lines are ship tracks, and the colors around them are ship-sampled SST. Ship and satellite SST are not identical because these were not measured at exactly the same times. The large and small open diamonds indicate the start of the Triaxus and MVP surveys on the *Oceanus* and *Endeavour*, respectively.



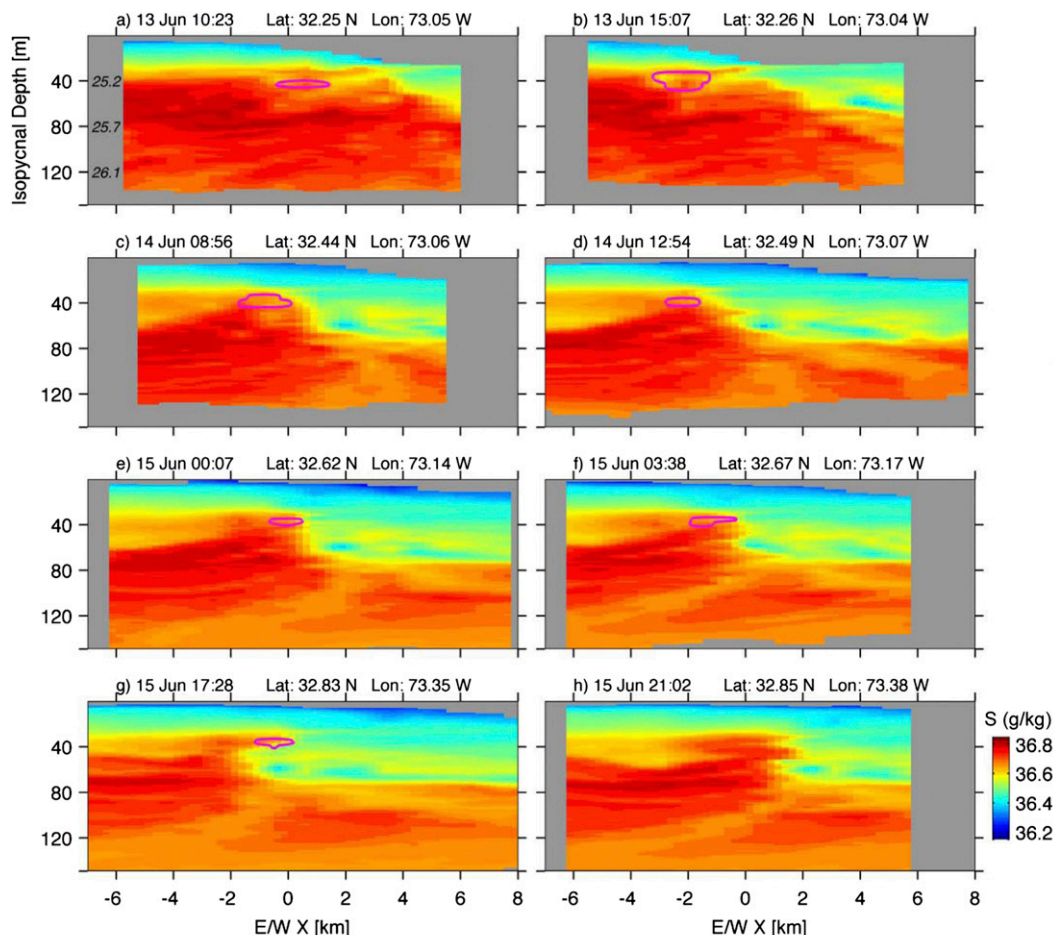


FIG. 3. MVP section time series showing the sharpening of a meridionally oriented water-mass front by  $\sim 0.1f$  confluence during 13–15 Jun 2011 at site 2. Plotted is salinity  $S$ . The vertical axis is average depth of an isopycnal  $\langle z(\rho) \rangle$  for the whole deployment with isopycnal densities at 40-, 80-, and 120-m depth indicated to the right of the left axis in (a). The horizontal axis is the zonal distance from the rhodamine dye centroid; the dye patch location is inscribed by the magenta contour [no dye was seen in (h)].

fluorescein filaments confirmed the target density, but these surveys were not designed to map the dye that will be reported elsewhere. Over the 10-m vertical aperture, water-mass variability (Fig. 3) was roughly coherent at site 2, although tilting or slumping was evident in the later site 2 surveys. The Acrobat tow body was primarily used to survey the dye but is included here because its Richard Branker Research (RBR) CTD allows the estimation of horizontal wavenumber spectra for salinity anomalies on isopycnals. It had a midvertical aperture horizontal resolution of about 150 m but also has smaller horizontal spacings at the crests and troughs of its vertical excursions.

#### 4. Spectral analysis methods

All four instrument platforms measured temperature, conductivity, and pressure. These were transformed into

isopycnal ( $\sigma_\theta$ ) temperature  $T$ , salinity  $S$ , and displacement  $\xi$  values. On density surfaces, temperature and salinity anomalies are equivalent measures of water-mass (spice; Veronis 1972) variability; spice anomalies are  $2\beta S'$ , where  $\beta = 7.5 \times 10^{-4} \text{ kg g}^{-1}$ . Here, we use salinity anomalies  $S'$  relative to each instrument's survey mean. These data will be used to synthesize a horizontal wavenumber spectrum  $S[S'](k)$  to span the meso- to finescale band (0.03–30-km horizontal wavelengths). By working on isopycnals, variability associated with internal-wave vertical displacements  $\xi$  is filtered out, but, as will be shown, internal-wave horizontal strain of the mesoscale along-isopycnal gradient may still contribute.

To compute spectra, Triaxus, MVP, and Acrobat salinity anomalies  $S'$  on isopycnals between average depths 30–60-m fast Fourier transformed in the meridional or zonal directions under the assumption that the sampling

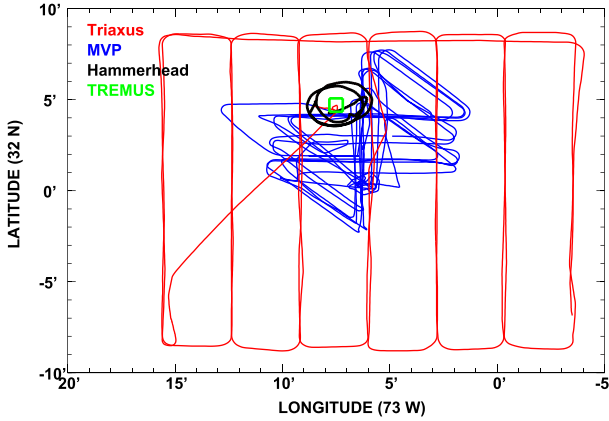


FIG. 4. Illustration representative of the nested sampling. Shown are 3 days at site 1 from the *Oceanus* (Triaxus, Hammerhead, and T-REMUS) and *Endeavour* (MVP). Triaxus measured a 35-km radiator grid (red), MVP made repeated 15-km butterfly surveys (blue), and Hammerhead was towed in 2-km radius circles (black loops) around 1-km T-REMUS boxes (green) centered on a drogued Gateway buoy at 32°5'N, 73°7'W.

was on a uniform grid, and then a  $\text{sinc}^2$  spectral correction applied. Long Triaxus lines were predominantly meridional, while MVP lines were both zonal and meridional (Fig. 3).

Since Hammerhead surveys were circles, a different procedure was used that was also applied to the T-REMUS box surveys. Locations were transformed into Lagrangian coordinates using the drogued Gateway buoy to reduce space–time aliasing; this made little difference at site 1 but aligned the site 2 frontal structure (Fig. 6). Temperature data were offset relative to

conductivity to correct for sensor lag in the computation of salinity. The raw Hammerhead data were smoothed over 20 s (125 points, 0.3-m depth, and 10 m laterally) to average over 10-s period pitching and heaving. Following linear interpolation of smoothed  $T$ ,  $S$ , and isopycnal displacement  $\xi$  signals onto a  $\sigma_\theta$  grid spanning 20–40-m depth, isopycnal salinity anomaly  $S'$  pairs were bin averaged to form covariances with respect to zonal  $\Delta x$  or meridional  $\Delta y$  separations, that is,  $\text{cov}[S'](|\Delta r|) = \langle S'(r)S'(r + \Delta r) \rangle$ . While each pair was confined to an isopycnal, bin averaging spanned the  $\sigma_\theta$  grid under the assumption of uniform statistics over the vertical aperture. For zonal spectra, meridional separations were restricted to  $\Delta y < 0.1\Delta x$  and, for meridional spectra,  $\Delta x < 0.1\Delta y$ . In addition, pair time separations  $\Delta t$  were restricted so that pairs spanning repeat tracks were not binned to further minimize space–time aliasing at small separations. The covariance approach takes advantage of the shorter spacings at the apexes and zeniths of the Hammerhead and T-REMUS vertical excursions (Fig. 5) to get smaller resolution than is possible with the MVP and Triaxus tow-yos. The resulting covariance function was then fit to cosines

$$a_n = \frac{2}{L \cos^2(k_n L)} \int_0^L \text{taper}(\Delta x) \text{cov}(\Delta x) \cos(k_n \Delta x) d\Delta x, \quad (1)$$

where  $L$  is the maximum pair separation with a sufficient number of pairs to produce stable covariances (typically 4–6 km),  $k_n = n\pi/L$  are 22 orthogonal wavenumbers (limited by the smoothing), and the  $\cos^2[\pi\Delta r/(2L)]$  taper

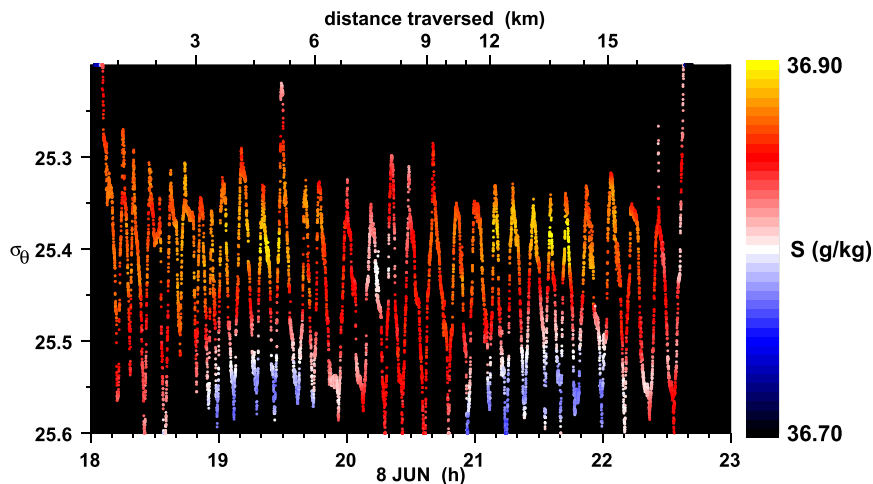


FIG. 5. Salinity  $S$  on isopycnals for the 8 Jun deployment of Hammerhead as a function of  $\sigma_\theta$  and time  $t$  with distance traversed along the upper axis. Two circuits were conducted roughly 2 h apart as evident from the repeated low salinities on isopycnals denser than 25.5 starting near 19 and 21 h.

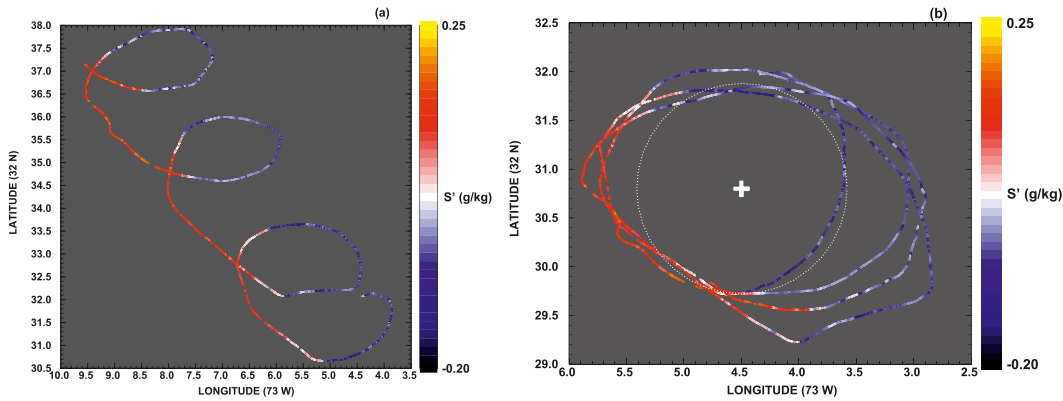


FIG. 6. Representative site 2 transformation from (left) Eulerian to (right) Lagrangian coordinates using the drogued Gateway buoy to center the Lagrangian coordinates ( $U = -0.25 \text{ m s}^{-1}$  and  $V = 0.45 \text{ m s}^{-1}$ ). This example shows the Hammerhead tow-yo path for its 14 Jun deployment.

ensures that the integrand goes to zero smoothly as  $\Delta r \rightarrow L$ . The spectrum is then computed from the fit coefficients  $a_n$ .

Fits to Bessel functions

$$a_n = \frac{2}{L^2 J_0^2(k_n L)} \int_0^L \text{taper}(\Delta r) \text{cov}(\Delta r) J_0(k_n \Delta r) \Delta r \Delta r, \quad (2)$$

as should be appropriate for isotropic 2D fields (D'Asaro and Perkins 1984), proved unable to capture the high-wavenumber part of the spectrum because the  $\Delta r$  weighting in the integral suppresses contributions from smaller  $\Delta r$ . The cosine-fitting routine (1) robustly reproduced both red and blue spectral slopes for artificial datasets with the same spatiotemporal sampling as the Hammerhead data, resolving slopes to better than  $\pm 0.1$ .

## 5. The tracer gradient spectra

For clarity of presentation of the spectral slopes, the horizontal wavenumber spectra for salinity (water-mass and spice) anomalies on isopycnals 20–60-m-deep (below a 10-m deep mixed layer base)  $S'[S'](k)$ , where horizontal wavenumber  $k$  is in cycles per kilometer (cpkm), were converted into salinity-gradient spectra by multiplying by  $4\pi^2 k^2$  (Figs. 7–9). Suspect MVP and Triaxus spectral estimates at the highest and lowest wavenumbers are not shown or used in the analysis. With less data, Hammerhead and T-REMUS spectra had to be averaged over both sites—as well as both zonally and meridionally—to produce statistically stable spectra; these have eight and seven independent realizations, respectively.

Salinity-gradient spectra (Fig. 7) are almost flat ( $k^0$ ) over 0.1–30 cpkm (horizontal wavelengths 0.03–10 km)

with least squares fit slopes of  $-0.2 \pm 0.2$  for Hammerhead, T-REMUS, and site 1 Triaxus, while the Acrobat spectrum at site 1 (thick solid magenta) may be slightly bluer with least squares fit slopes of  $0.0 \pm 0.2$ . The Hammerhead and T-REMUS data extend the spectrum for passive tracer on isopycnals about an order of magnitude higher than most previously reported [the wavelet analysis of Ferrari and Rudnick (2000) extended to wavelengths as small as 10 m (R. Ferrari 2014, personal communication), but these were not reported]. Where they overlap, spectra from the different platforms agree closely despite different instruments,

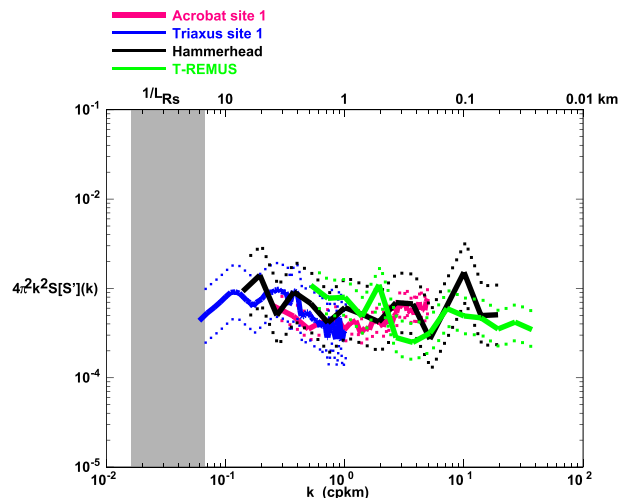


FIG. 7. Horizontal wavenumber spectra of salinity gradients on isopycnals from the four instruments  $4\pi^2 k^2 S'[S'](k)$  with the highest resolution (thick solid lines; magenta is Acrobat site 1; Triaxus site 1 is blue; Hammerhead is green; T-REMUS is green) along with 95% confidence limits of these means (thin dotted lines). Hammerhead and T-REMUS have been averaged over both sites as well as meridionally and zonally for statistical stability. The gray bar to the left is the predicted range of Rossby wavenumber [3].

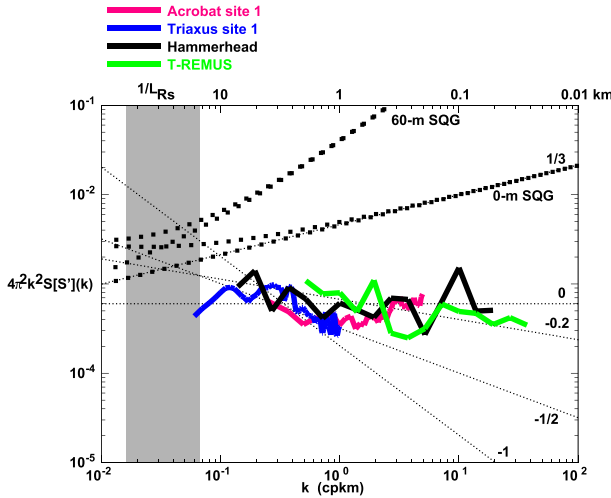


FIG. 8. Comparison of the horizontal wavenumber spectra for salinity gradient on isopycnals  $4\pi^2 k^2 S[S'](k)$  (thick solid lines) with surface quasigeostrophic turbulence theory predictions (thick black dotted curves) at the surface (0-m SQG,  $k^{1/3}$ ) and upper pycnocline (60-m SQG), for which a  $k^1$  Batchelor spectrum is predicted above the Rossby wavenumber (left gray shading). At low wavenumbers, the theoretical spectra split into  $k^{1/3}$  as predicted by quasigeostrophic theory and  $k^0$  as expected for frontogenesis. Slopes of  $-1$ ,  $-1/2$ ,  $-0.2$ ,  $0$ , and  $+1/3$  (thin dotted lines) are labeled inside the panel for reference where the  $+1/3$  line overlaps the surface curve (0-m SQG).

measurement locations, processing, and spectral methods. Kinematically, a  $k^0$  (flat) gradient spectrum is consistent with a step or front for scales larger than the front's width (Jenkins and Watts 1968),  $k^{0-2}$  for multiple fronts or filaments and  $k^2$  for white noise. Thus, the observed nearly flat spectra (Fig. 7) are consistent with the presence of isolated salinity fronts no wider than  $\lambda_h/(2\pi) \sim 5$  m at both sites, though no distinct front was evident at site 1. Other explanations cannot be ruled out as presented in section 7.

All the observed spectra are redder, that is, have more negative slopes, than the predicted  $k^1$  Batchelor gradient spectrum for SQG above the Rossby wavenumber (thick black dotted curves; Fig. 8); because our spectra are in the pycnocline rather than at the surface (0-m SQG curve in Fig. 8), the 60-m SQG spectrum of  $k^1$  in Fig. 8 should apply (Scott 2006), and the appropriate SQG Rossby wavenumbers are at the lower end of our spectral bandwidth (gray band in Fig. 8). However, with slopes of  $-0.2 \pm 0.2$ , the observed spectra are redder even than the gentler  $k^{1/3}$  theoretical quasigeostrophic spectrum that applies at the surface (0-m SQG in Fig. 8). Redder spectra signify a more rapid cascade of variance to high  $k$  so that additional submesoscale shear must contribute to stirring in this wavenumber band than predicted by quasigeostrophic theories.

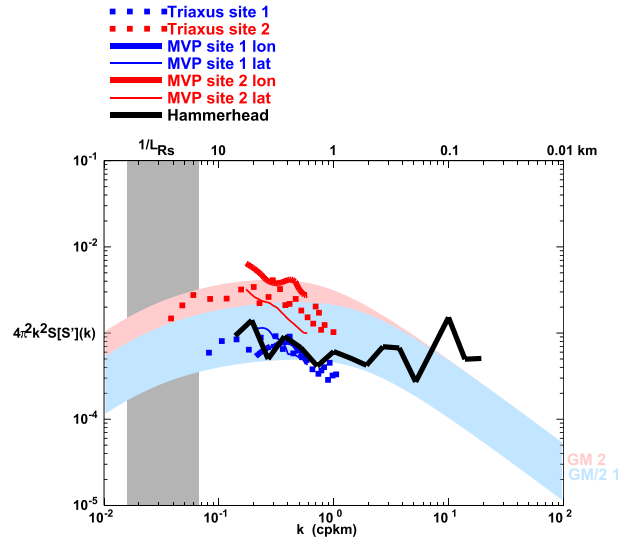


FIG. 9. Comparison of horizontal wavenumber spectra for salinity gradients along isopycnals  $4\pi^2 k^2 S[S'](k)$  at site 1 (dark blue) and site 2 (red), zonal (thick solid) and meridional (thin solid and thick dotted). The Hammerhead spectrum (black) is shown for reference and appears to be dominated by site 1 levels in the wavenumber band that overlaps with the MVP and Triaxus spectra. Colored curving bands correspond to model spectra for internal-wave horizontal strain normalized with the corresponding site salinity-gradient variances (light blue, GM/2 at site 1; pink, GM/2 at site 2).

At site 2, MVP and Triaxus find a factor of 4 higher levels than site 1 (Fig. 9) because of higher salinity variability associated with the water-mass front (Figs. 3, 6). Furthermore, the site 2 MVP zonal spectrum is higher than the meridional spectrum, consistent with the front's orientation; higher spectral levels for the site 2 zonal spectra were also found by Hammerhead and T-REMUS but were not robust (not shown). The average Hammerhead spectrum shown appears to be biased to site 1 levels based on its similarity to site 1 Triaxus, MVP, and Acrobat spectra. MVP and Triaxus spectra (Fig. 9) are redder with slopes near  $-1$  to  $-1/2$  over the  $0.2$ – $0.7$ -cpkm band, but this wavenumber band is too narrow to obtain reliable slopes, and it may be better to interpret this as a drop in the passive tracer spectral level; a drop in passive tracer spectral level would imply a stronger cascade, as might arise from elevated shear in this wavenumber band. The Triaxus spectrum may be weakly blue with slopes about  $+1/3$  for  $k < 0.2$  cpkm, but, again, this wavenumber band is too narrow for the slopes to be robust.

## 6. Comparison with other observed submesoscale tracer spectra

The gradient passive tracer spectra reported here are almost flat with slopes  $-0.2 \pm 0.2$  over the submesoscale

wavenumber range  $0.1 < k < 30$  cpkm (Figs. 7–9). However, we have only two to three independent realizations of the ocean eddy field. In this section, we summarize the literature on gradient passive tracer spectra along isopycnals. Though these measurements are mostly for wavenumbers  $k < 1$  cpkm, they still are above the Rossby wavenumber. These have consistently reported redder (more negative slopes) than  $k^1$  in the submesoscale range. Most of these studies are based on dozens or hundreds of independent realizations of the submesoscale so lend more robust support to our conclusions.

Based on wavelet analysis of SeaSoar data in the central North Pacific, Ferrari and Rudnick (2000) reported white spice gradient spectra on wavelengths of 0.5–10 km ( $\sim 0.1$ –2 cpkm; converting their wavelet estimates to wavenumber spectra), consistent with the almost flat spectral shape reported here (Fig. 7). Cole et al. (2010) found flat or slightly blue gradient spectra for wavenumbers below our resolution,  $k < 0.03$  cpkm in the subtropical North Pacific, showing that similarly flat spectra are found at lower wavenumbers. Callies and Ferrari (2013) report almost flat gradient spectra in the North Pacific. In 2 yr of central subtropical North Pacific glider data, Cole and Rudnick (2012) report  $k^0$  gradient spectra for  $0.003 < k < 0.06$  cpkm to depths of 800 m, sufficiently deep that surface quasigeostrophy should not raise the Rossby wavenumber. Klymak et al. (2015) found blue spice gradient spectra with slopes of 0.1–1 over 0.01–0.25 cpkm in the summer eastern subpolar gyre of the North Pacific, and slopes of 0.25–0.55 in the summer central subtropical gyre north of Hawaii. Their shallow spectra were bluer, while 120–170-m depth spectra were redder (slopes 0.1–0.3), inconsistent with the predicted change in spectral slope with depth for surface quasigeostrophy in the submesoscale band as it transitions from  $k^{1/3}$  or  $k^0$  below the surface Rossby wavenumber to  $k^1$  at the depth of the Batchelor range above the interior Rossby wavenumber (Fig. 8; Scott 2006). They reported vertically coherent eddies of nonlocal origin contributing to their spectra; coherent eddy features are not included in homogeneous quasigeostrophic turbulence theory, and none were evident in our surveys.

## 7. Discussion

Salinity-gradient spectra from the seasonal pycnocline at two sites in the summer Sargasso Sea with weak and moderate eddy confluence were resolved for submesoscale horizontal wavenumbers  $k = 0.1$ –30 cpkm (horizontal wavelengths 0.3–10 km) using nested tow-yo and autonomous surveys (Figs. 7–9). These spectra have

slopes of  $-0.2 \pm 0.2$  over the resolved wavenumber range and so are flat to first approximation. A flat gradient spectrum is consistent with a front no wider than the smallest resolved length scales  $\ell \sim \lambda/(2\pi) \sim O(5)$  m. The 1–10-km  $\sim 0.1f$  confluences at site 2 could sharpen gradients over 10 km down to the smallest resolved scales in 5–10 days, but there must be additional submesoscale confluences acting on length scales smaller than 1–5 km to explain an almost flat observed spectra. No coherent front was evident at site 1.

Since the  $0.1f$  confluences would cascade variance through the observed submesoscale wavenumber range in only a week or so, submesoscale water-mass variability is transient and requires a continuous supply of variance to maintain it. In the upper pycnocline we sampled, it might be (i) relict structure left behind as the winter mixed layer shoaled (Cole et al. 2010), (ii) subduct at fronts (Mahadevan 2006), or (iii) cascade from mesoscale water-mass variability by any of a number of stirring mechanisms that we examine below.

### a. Unlikely explanations

#### WE CAN RULE OUT EIGHT POSSIBLE EXPLANATIONS FOR A FLAT GRADIENT SPECTRUM

##### (i) Relict winter mixed layer variability

As mentioned above,  $\sim 0.1f$  confluence would cascade variance through and out of the submesoscale wavenumber band in  $O(10)$  days. Examination of Argo profiling float data in  $32^\circ$ – $33^\circ$ N,  $71^\circ$ – $74^\circ$ W suggests that the winter mixed layer shoals above 20-m depth by late April, more than 40 days before our measurements commenced. Thus, for our measurements in the seasonal pycnocline in June, enough time has passed for submesoscale water-mass anomalies left behind by the shoaling winter mixed layer to cascade out of our wavenumber domain.

##### (ii) Quasigeostrophic turbulence

As already mentioned, nearly flat gradient spectra in the 0.03–10-cpkm wavenumber range are not consistent with quasigeostrophic turbulence theories (Fig. 8; e.g., Charney 1971; Scott 2006) that predict a blue  $k^1$  Batchelor (1959) gradient spectrum above the shear-containing wavenumber. A Batchelor spectrum arises at wavenumbers higher than the wavenumber of the dominant straining (nonlocal spectrally) that, for quasigeostrophy, is the baroclinic mode-one Rossby wavenumber  $f/(NH)$  or lower, that is, well below our survey resolution. Quasigeostrophic numerical simulations (Smith and Ferrari 2009) confirm  $k^1$  gradient spectra above the Rossby wavenumber.



Surface quasigeostrophic turbulence theory (Scott 2006) predicts gradient spectral slopes of 0–0.3 below the surface Rossby wavenumber

$$k_R(z) = 1/[2\pi L_s(z)] \quad \text{where} \quad L_s(z) = \int_z^0 [N(z') dz'/f] \quad (3)$$

or lower and a  $k^1$  Batchelor spectrum at higher wavenumbers. As the surface Rossby wavenumber decreases with depth [(3)], the predicted submesoscale spectrum becomes bluer with depth. The surface Rossby wavenumber at 20–60-m depth is at the low end of our resolved wavenumber band ( $k = 0.02$ – $0.07$  cpkm; gray bands in Figs. 7–9).

Thus, observed submesoscale tracer gradient spectra are redder; that is, they have a more negative slope, extending to higher wavenumber (Fig. 7; Ferrari and Rudnick 2000; Cole et al. 2010; Callies and Ferrari 2013; Klymak et al. 2015) and greater depth (Cole and Rudnick 2012), than can be explained by quasigeostrophic theories (Charney 1971; Scott 2006). An observed spectrum redder than the  $k^1$  Batchelor spectrum suggests that there is significant horizontal shear on length scales smaller than the Rossby deformation scale accelerating the cascade to smaller scales. Drifter pair spreading also finds significant submesoscale shear (Lumpkin and Elipot 2010; Poje et al. 2014).

#### (iii) Nocturnal mixed layer deepening

Nocturnal mixing extends no deeper than 30-m depth during the nights of 15 and 19 June at site 2 based on Electromagnetic Autonomous Profiling Explorers (EM-APEX) float temperature variance dissipation rate  $\chi_T$  microstructure measurements (Shcherbina et al. 2015) and so will not impact our deeper measurements.

#### (iv) Unrepresentative sampling

The 2–3 realizations described here may capture an unrepresentative part of the field that does not reflect the full eddy statistics, that is, represent a spatial inhomogeneity. Neither sites 1 nor 2 had significant vorticity, and site 2 was centered on a confluence that is expected to sharpen mesoscale water-mass variability into a front with a  $k^0$  gradient spectrum (Hoskins and Bretherton 1972). However, similar spectral slopes are reported from much more extensive measurements, as presented in section 6, which were not so biased (Ferrari and Rudnick 2000; Cole and Rudnick 2012; Callies and Ferrari 2013; Klymak et al. 2015), albeit mostly at lower wavenumbers  $k < 1$  cpkm. Thus, we view our spectral slopes as likely to be representative.

#### (v) Finescale potential vorticity anomalies

The vortical mode (stratified turbulence) may be generated by breaking near-inertial waves. Turbulent

patches often share the low aspect ratios of finescale, near-inertial waves (Marmorino et al. 1986; Marmorino et al. 1987; Itsweire et al. 1989), and turbulent patches during the Lateral Mixing measurements were coherent over at least 1 km laterally and so are in the right wavenumber band. Numerical simulations of stratified turbulence (Brethouwer and Lindborg 2008) predict an inertial subrange  $k^{1/3}$  passive tracer gradient spectra for the downscale (toward higher wavenumber) cascade and so cannot explain the almost flat observed spectra for  $k > 1$  cpkm (Figs. 7–8).

#### (vi) Nonstationarity or inhomogeneity

Unlike the usual assumptions of quasigeostrophic turbulence theories and models, the ocean's subinertial eddy field is nonstationary or inhomogeneous. For example, Klymak et al. (2015) reported coherent eddies of California Undercurrent Water in the eastern subpolar North Pacific, likely spun off of topographic features along the eastern boundary (Pelland et al. 2013). Reported variability in observed submesoscale spectral slopes (Klymak et al. 2015; Callies and Ferrari 2013) may be in part a signature of these features. If so, they would be common given the other observations of a  $k^0$  spectrum. Isolated coherent eddies were not evident in any of our Sargasso Sea surveys.

#### (vii) Submesoscale frontal subduction

Strong, along-isopycnal vertical velocities can arise at submesoscale fronts to drive subduction of surface-layer variability into the upper pycnocline (Mahadevan 2006). Since this exchange is along isopycnals, it can extend no deeper than the densest water in the mixed layer. This may explain Cole et al. (2010) and Todd et al. (2012) reporting layers of elevated submesoscale water-mass variability in the seasonal pycnocline persisting late into summer. The larger-scale Triaxus surveys found the densest water at 20-m depth to be  $\sigma_\theta = 25.3933 \text{ kg m}^{-3}$ . The deepest that such densities found are 58 m, which is in the range where the spectra were made. However, subducted mixed layer water should be of low potential vorticity (stratification) (Spall 1995), while the stratification in the two surveyed sites in the seasonal pycnocline was uniformly high ( $N \sim 10^{-2} \text{ s}^{-1}$ ). Further, the presence of similar submesoscale spectral slopes in 800-m deep layers beyond the reach of subduction (Cole and Rudnick 2012) suggests a common cause that, in their case, can only be cascading of water-mass variance into the submesoscale by the stirring of larger-scale gradients. Therefore, while we cannot rule out subduction, we think it unlikely.

#### (viii) Horizontal mixing

An isopycnal diffusivity  $K_h$  would be expected to cause a steep rolloff at high horizontal wavenumbers. No

such steeply red rolloff is evident in our wavenumber band (Fig. 7). Further, the rolloff wavenumber  $k_R$  should be

$$k_R = 2\pi \sqrt{\frac{\alpha}{K_h}}, \quad (4)$$

where  $\alpha$  is the confluence. D. A. Birch et al. (2014, unpublished manuscript) report dye horizontal diffusivities  $K_h = 0.8\text{--}0.9 \text{ m}^2 \text{ s}^{-1}$  at both sites, which will include diapycnal mixing through shear dispersion and 1–10-km confluences of  $(1.5\text{--}3.0) \times 10^{-6} \text{ s}^{-1}$  at site 1 and  $15 \times 10^{-6} \text{ s}^{-1}$  for the first day at site 2, dropping to  $10^{-6} \text{ s}^{-1}$  for the subsequent 6 days. At higher wavenumbers, the rms confluence is expected to increase because of additional submesoscale shearing contributions from those wavenumbers. Likewise, the horizontal diffusivity is expected to decrease. Therefore, a rolloff wavenumber based on the above numbers will be a lower bound; indeed, scaling with the Okubo (1971) horizontal diffusivity diagram suggests that the rolloff wavenumber will increase faster than the wavenumber at which the diffusivity and confluence are estimated, suggesting that other processes must ultimately arrest the cascade of variance. Nevertheless, the above numbers imply rolloff wavenumbers  $k_R = 5\text{--}25 \text{ cpkm}$  that are at the high-wavenumber end of our spectrum. Since no steep rolloff is present in this wavenumber band in our spectra (Fig. 7), this mechanism seems unable to explain the almost flat submesoscale spectrum.

#### b. Possible explanations

TWO REMAINING MECHANISMS MAY BE ABLE TO EXPLAIN ALL OR PART OF THE SUBMESOSCALE PASSIVE TRACER SPECTRUM

##### (i) Nonquasigeostrophic subinertial stirring

Subinertial shears are not limited by the Rossby deformation wavenumber  $f/(NH)$ , as in quasigeostrophic turbulence theory, but may have contributions from many vertical wavenumbers or modes just as in internal gravity waves. Primitive equation numerical simulations confirm that strong shears develop on the submesoscale at surface and interior fronts (Klein et al. 2008; Capet et al. 2008b; Molemaker et al. 2010) perhaps accessible with semigeostrophy (Hoskins and Bretherton 1972; Blumen 1978). Moreover, these frontal shears penetrate deeper than predicted by surface quasigeostrophic turbulence theory. In primitive equation simulations of the California Current System, Capet et al. (2008a) reported that tracer gradient spectra at fixed depths were flat at all depths, even though HKE and APE transitioned from  $k^{-2}$  at the surface to  $k^{-1}$  at depth consistent with quasigeostrophic

theory. Tulloch et al.'s (2011) eddy-resolving numerical simulations revealed that, in weak baroclinic eddy fields without the deep PV gradient reversal that characterizes western boundary currents (i.e., conditions that typify the Sargasso Sea and North Pacific gyres), baroclinic instabilities fill out the submesoscale. Primitive equation simulations of the Eady problem (zero interior potential vorticity gradients) found a nonquasigeostrophic forward cascade associated with frontogenesis, frontal instability, and dissipation in the interior as well as at the surface (Capet et al. 2008b; Molemaker et al. 2010) and indicated that quasigeostrophic dynamics were fundamentally insufficient to describe the submesoscale even though most of the energy and domain were in quasigeostrophic and hydrostatic balance.

##### (ii) Internal-wave horizontal strain

Submesoscale salinity variability on isopycnals is a result of horizontal strain deforming large-scale salinity gradients just as vertical strain deforms the vertical density profile. As previously noted, internal waves dominate dynamic signals over the resolved range of horizontal wavenumbers. While reversible on time scales that are short compared to balanced shears, internal waves induce  $O(1)$  horizontal strains  $\int u_x dt$ ,  $\int u_y dt$ ,  $\int v_x dt$ , and  $\int v_y dt$  (see the appendix) that will deform any large-scale background property gradient on isopycnals from conservation of salinity

$$\frac{\partial(S_x, S_y)}{\partial t} = -(u_x \bar{S}_x + v_x \bar{S}_y, u_y \bar{S}_x + v_y \bar{S}_y). \quad (5)$$

Integrating with time yields

$$(S_x, S_y) = -\left(\bar{S}_x \int u_x dt + \bar{S}_y \int v_x dt, \bar{S}_x \int u_y dt + \bar{S}_y \int v_y dt\right). \quad (6)$$

Taking into account the rolloff at  $\sim O(10) \text{ m}$  vertical wavelength (Gargett et al. 1981), and that internal-wave energy was half Garrett–Munk (GM) levels at site 1, the horizontal wavenumber spectrum for horizontal strain from a canonical model spectrum (see the appendix) is multiplied by the observed salinity-gradient variance to obtain a spectrum of internal-wave-induced salinity-gradient variability. The resulting spectrum can explain the observed spectra for  $k < 7 \text{ cpkm}$  at both sites (Fig. 9) but rolls off too steeply at the higher wavenumbers captured by Hammerhead and T-REMUS ( $7 < k < 30 \text{ cpkm}$ ); it also falls short of the site 2 zonal spectrum because of the front (Fig. 3). While the high vertical wavenumber  $m$  high-frequency  $\omega$  part of the internal-wave spectrum that contributes to the high horizontal wavenumber  $k$  part of the spectrum is arguably not well

known, a number of plausible modifications to the GM model proved unable to reproduce the high  $k$  level and shape of the observed spectrum, including (i) enhancing the inertial peak by  $[\omega^2/(\omega^2 - f^2)]^{1/3}$  (Kunze et al. 2006); (ii) adding a near-inertial peak between  $\omega = 1.05\text{--}1.10f$ ; (iii) allowing the rolloff wavenumber  $m_c$  to increase with  $\omega$  as an alternative explanation for the increasing shear/strain variance ratio for increasing  $m > m_c$  (Polzin et al. 2003); and (iv) multiplying the overall spectrum by  $\omega/f$ , though this last is inconsistent with recent high vertical wavenumber  $m$  profiles of vertical velocity  $w$  (Thurnherr et al. 2015, manuscript submitted to *Geophys. Res. Lett.*). Only dynamically inconsistent changes to the GM model spectrum (e.g., Richardson number  $Ri \ll 0.25$ ) could reproduce a flat gradient spectrum for  $k$  above 1 cpkm. Therefore, internal-wave horizontal strain may contribute to the observed submesoscale spectrum for  $k < 7$  cpkm but not at the highest wavenumbers resolved by Hammerhead and T-REMUS.

## 8. Conclusions

Our measurements find an almost flat spectrum for salinity (water-mass and spice) gradients along isopycnals with spectral slopes of  $-0.2 \pm 0.2$  over submesoscale horizontal wavelengths 0.03–10 km (Figs. 7–8). This is consistent with water-mass fronts (Hoskins and Bretherton 1972), though no coherent front was evident at site 1. It is not consistent with quasigeostrophy (Charney 1971; Scott 2006; Smith and Ferrari 2009) that predicts a  $k^1$  Batchelor spectrum above the Rossby deformation wavenumber (Fig. 8). While we cannot rule out that our sampling does not fully characterize the Sargasso Sea submesoscale field, particularly with its focus on a confluence at site 2, previous more extensive measurements (Ferrari and Rudnick 2000; Cole and Rudnick 2012; Callies and Ferrari 2013; Klymak et al. 2015) support a redder submesoscale gradient spectrum than quasigeostrophic turbulence theories predict as being representative. While these are mostly at lower horizontal wavenumbers than resolved here, unreported results from the Ferrari and Rudnick (2000) measurements support the flat gradient spectra at the highest wavenumbers resolved by Hammerhead and T-REMUS (Fig. 7).

Thus, there is more in the ocean than dreamt of in quasigeostrophy. Additional submesoscale shearing must be present on these scales. This conclusion has also been reached from drifter studies (Lumpkin and Elipot 2010; Poje et al. 2014) and primitive equation numerical simulations (Capet et al. 2008a,b; Tulloch et al. 2011). While quasigeostrophic models find a  $k^1$  spectrum at high wavenumbers (Smith and Ferrari 2009), primitive equation numerical simulations reproduce the observed

$k^0$  spectrum (Fig. 7), albeit at fixed depths that can include vertical displacements rather than along isopycnals, nevertheless pointing to additional nonquasigeostrophic stirring on the submesoscale being responsible for the observed spectral slopes. Molemaker et al. (2010) report that unbalanced motions are important for a submesoscale forward cascade, even though they represent a small fraction of the model domain and energy.

As well as ruling out quasigeostrophic stirring, (i) submesoscale relict mixed layer anomalies should be stirred out of the submesoscale wavenumber band on time scales short compared to the spring shoaling of the mixed layer above 20 m, (ii) nocturnal mixing did not extend deep enough, and (iii) a downscale vortical-mode (stratified turbulence) cascade would produce a  $k^{1/3}$  spectrum (Brethouwer and Lindborg 2008) that is too blue, allowing us to rule out these mechanisms. Horizontal mixing, including diapycnal mixing coupled with shear dispersion, would act to steeply redden the spectrum at wavenumbers above those resolved. While submesoscale subduction (Mahadevan 2006) cannot be ruled out in our measurements, the absence of low potential vorticity (stratification) anomalies argues against subducted mixed layer water. As well, Cole and Rudnick (2012) report similarly flat spectra as deep as 800 m, where the only source of submesoscale water-mass variance is a cascade from larger scales. And Capet et al. (2008a) find flat tracer gradient spectra independent of depth, albeit on depth not isopycnal surfaces. Our similar slopes (Fig. 7) suggest a submesoscale stirring mechanism in common.

Equally, a number of mechanisms cannot be ruled out as explanations for parts of the observed almost flat salinity-gradient spectrum based on available information. Internal waves may account for the low-wavenumber band  $0.1 < k < 7$  cpkm (Fig. 9) but have slopes that are too red at the highest wavenumbers resolved by Hammerhead and T-REMUS. Thus, internal waves appear to dominate passive tracer signals on isopycnal signals as well as dynamic signals in the submesoscale band. Internal waves cannot explain the extension of the almost flat gradient spectrum to finescale wavenumbers of  $7 < k < 30$  cpkm (Fig. 9).

With observations of the subinertial submesoscale limited to passive tracer signals such as water-mass (spice) anomalies because of the dominance of internal-wave HKE and APE on these scales, and even passive tracers showing the influence of internal gravity wave horizontal strain (Fig. 9; see the appendix), submesoscale primitive equation numerical models appear to be the best means of teasing apart the dynamics controlling the passive tracer spectrum over  $0.1 < k < 100$  cpkm.

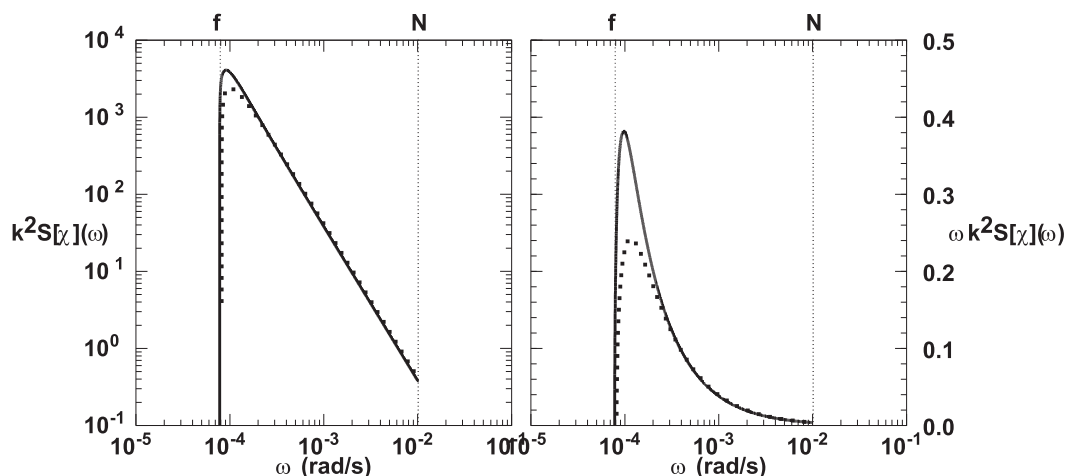


FIG. A1. Frequency  $\omega$  spectrum for horizontal strain  $\chi_h$  (solid) and vertical strain  $\xi_z$  (dotted) in (left) log–log and (right) variance-preserving forms from the Garrett–Munk model spectrum. The spectra peak near  $\omega = 1.35f$  and falls off as  $\omega^{-2}$ .

Subinertial frontogenesis  $O(1)$  or higher Rossby number shears and the secondary adjustment circulations that set up to restore balance seem likely candidates at high  $k$  with statistical homogeneity, but nonlocal processes such as the subduction of mixed layer anomalies or formation of coherent eddies may also play a role. More, deeper measurements would help confirm that an almost flat tracer gradient spectrum is widespread and independent of depth. Finer horizontal resolution measurements on isopycnals might capture the high-wavenumber rolloff due to horizontal diffusion.

*Acknowledgments.* We thank the reviewers for helping to improve the paper. E. Kunze’s participation in the Office of Naval Research Lateral Mixing

Directed Research Initiative’s 2011 cruise was supported by ONR Grant N00014-08-1-0700 and subsequent analysis under N00014-12-1-0942. J. Klymak was supported by ONR Award N00014-11-1-0165, R. Ferrari was supported by N00014-09-1-0633, R.-C. Lien was supported by N00014-09-1-0193, C. Lee was supported by N00014-09-1-0266, M. Sundermeyer was supported by N00014-09-1-0194, and L. Goodman was supported by N00014-09-1-0173. Chris MacKay and Kevin Bartlett played invaluable roles in the collection of the Hammerhead data. Jason Gobat, Ben Jokinen, David Winkel, and Andrey Shcherbina were instrumental in the success of the Triaxus operations and data processing. This paper is in memory of Murray Levine, respected and beloved colleague.

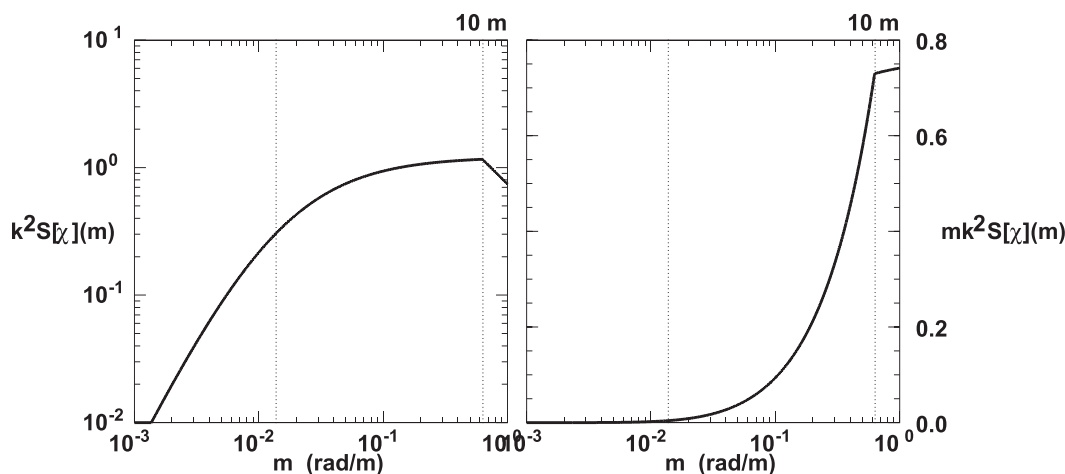


FIG. A2. Vertical wavenumber  $m$  spectrum for horizontal strain  $\chi_h$  in (left) log–log and (right) variance-preserving forms from the Garrett–Munk model spectrum.



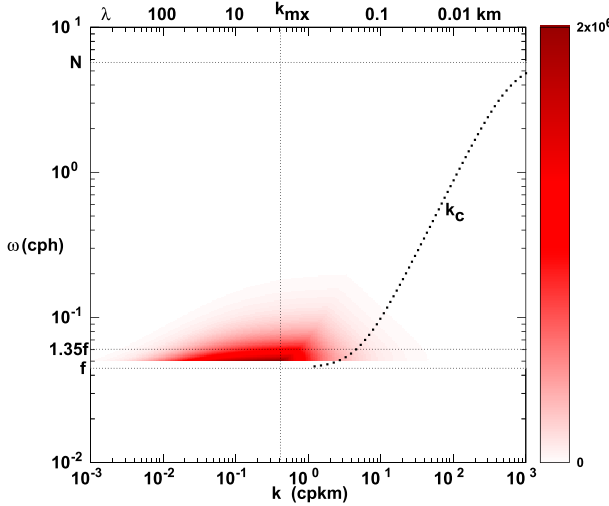


FIG. A3. Contour plot of the Garrett–Munk model spectrum for horizontal strain  $S[\chi_h](\omega, k)$  [(A2)] as a function of frequency  $\omega$  and horizontal wavenumber  $k$  showing the peak near  $f$  and a horizontal wavelength of 10 km. The rolloff horizontal wavenumber  $k_c = m_c(\omega^2 - f^2)^{1/2}/(N^2 - \omega^2)^{1/2}$  is plotted as a dotted curve. The vertical dotted line corresponds to the peak horizontal wavenumber of the horizontal strain spectra.

## APPENDIX

### The GM Horizontal Strain Spectrum

Horizontal strain  $\chi_h$  is the horizontal derivative of the horizontal deformation  $\chi$  and the time integral of the horizontal confluence  $[(u_x - v_y)^2 + (v_x + u_y)^2]^{1/2}$  that reduces to  $(u_x^2 + v_x^2)^{1/2}$  in a coordinate system where  $x$  is aligned with the horizontal wavevector  $\mathbf{k}$ . The Garrett–Munk 1976 model spectrum (Gregg and Kunze 1991) for horizontal strain in terms of frequency  $\omega$  ( $\text{rad s}^{-1}$ ) and vertical wavenumber  $m$  ( $\text{rad m}^{-1}$ ) is  $S[\chi_h](\omega, m) = k^2 S[\chi](\omega, m) = 2(k^2/\omega^2)S[\text{HKE}](\omega, m)$  and can be expressed as

$$S[\chi_h](\omega, m) = \pi E_0 f b j^* \left[ \frac{(\omega^2 + f^2)\sqrt{\omega^2 - f^2}}{\omega^5} \right] \left[ \frac{m^2}{(m + m^*)^2} \right], \quad (\text{A1})$$

(Figs. A1–A2) where nondimensional spectral level  $E_0 = 6.3 \times 10^{-5}$ ;  $f$  is the Coriolis frequency; pycnocline stratification length scale  $b = 1300$  m; peak mode number  $j^* \sim 3$  at midlatitude; and low-mode peak vertical wavenumber  $m^* = \pi N j^*/(N_0 b)$ . At high wavenumbers,  $m > m_c = 0.2\pi/(E_0/E) \text{ rad m}^{-1}$ , and (A1) must be further multiplied by  $m_c/m$  to reflect the finescale vertical wavenumber rolloff (Fig. A2) (Gargett et al. 1981). This spectrum closely resembles that for vertical strain  $\xi_z$  and has variance  $O(1)$ . It is weighted toward low frequency,

peaking near  $1.35f$  (Fig. A1), and the rolloff vertical wavenumber  $m = m_c$  (Fig. A2). For  $\omega \gg f$ , the frequency spectrum falls off as  $\omega^{-2}$  (Fig. A1). Substituting for  $m^*$  and the hydrostatic wavenumber relation  $m = Nk/\sqrt{\omega^2 - f^2}$  and  $dm = Ndk/\sqrt{\omega^2 - f^2}$ , (A1) becomes

$$S[\chi_h](\omega, k) = \pi E_0 N N_0^2 f b^3 j^* \left( \frac{\omega^2 + f^2}{\omega^5} \right) \left[ \frac{k^2}{(k N_0 b + \pi \sqrt{\omega^2 - f^2} j^*)^2} \right], \quad (\text{A2})$$

which is nonseparable in horizontal wavenumber  $k$  and frequency  $\omega$  (Fig. A3). Numerically integrating frequency from  $f$  to  $N$ , and accounting for the rolloff for  $m > m_c$  and converting wavenumber  $k$  from radians per meter to cycles per kilometer, produces a horizontal wavenumber  $k$  spectrum (Fig. 9) with a peak near 1 cpkm.

## REFERENCES

- Batchelor, G. K., 1959: Small-scale variation of convected quantities like temperature in turbulent fluid. Part 1. General discussion and the case of small conductivity. *J. Fluid Mech.*, **5**, 113–133, doi:10.1017/S002211205900099X.
- Blumen, W., 1978: Uniform potential vorticity flow: Part I. Theory of wave interactions and two-dimensional turbulence. *J. Atmos. Sci.*, **35**, 774–783, doi:10.1175/1520-0469(1978)035<0774:UPVFPI>2.0.CO;2.
- Boccaletti, G., R. Ferrari, and B. Fox-Kemper, 2007: Mixed-layer instabilities and restratification. *J. Phys. Oceanogr.*, **37**, 2228–2250, doi:10.1175/JPO3101.1.
- Brethouwer, G., and E. Lindborg, 2008: Passive scalars in stratified turbulence. *Geophys. Res. Lett.*, **35**, L06809, doi:10.1029/2007GL032906.
- Callies, J., and R. Ferrari, 2013: Interpreting energy and tracer spectra of upper-ocean turbulence in the submesoscale range (1–200 km). *J. Phys. Oceanogr.*, **43**, 2456–2474, doi:10.1175/JPO-D-13-063.1.
- Capet, X., J. C. McWilliams, M. J. Molemaker, and A. F. Shchepetkin, 2008a: Mesoscale to submesoscale transition in the California Current System. Part I: Flow structure, eddy flux, and observational tests. *J. Phys. Oceanogr.*, **38**, 29–43, doi:10.1175/2007JPO3671.1.
- , —, —, and —, 2008b: Mesoscale to submesoscale transition in the California Current System. Part III: Energy balance and flux. *J. Phys. Oceanogr.*, **38**, 2256–2269, doi:10.1175/2008JPO3810.1.
- Charney, J. G., 1971: Geostrophic turbulence. *J. Atmos. Sci.*, **28**, 1087–1095, doi:10.1175/1520-0469(1971)028<1087:GT>2.0.CO;2.
- Cole, S. T., and D. L. Rudnick, 2012: The spatial distribution and annual cycle of upper ocean thermohaline structure. *J. Geophys. Res.*, **117**, C02027, doi:10.1029/2011JC007033.
- , —, and J. A. Colosi, 2010: Seasonal evolution of upper-ocean horizontal structure and the remnant mixed layer. *J. Geophys. Res.*, **115**, C04012, doi:10.1029/2009JC005654.
- D’Asaro, E. A., and H. Perkins, 1984: The near-inertial internal wave spectrum in the late summer Sargasso Sea. *J. Phys. Oceanogr.*, **14**, 489–505, doi:10.1175/1520-0485(1984)014<0489:ANIWS>2.0.CO;2.

- Ferrari, R., and D. L. Rudnick, 2000: Thermohaline variability in the upper ocean. *J. Geophys. Res.*, **105**, 16 857–16 883, doi:[10.1029/2000JC900057](https://doi.org/10.1029/2000JC900057).
- , and K. L. Polzin, 2005: Finescale structure of the  $T$ – $S$  relation in the eastern North Atlantic. *J. Phys. Oceanogr.*, **35**, 1437–1454, doi:[10.1175/JPO2763.1](https://doi.org/10.1175/JPO2763.1).
- Gargett, A. E., P. J. Hendricks, T. B. Sanford, T. R. Osborn, and A. J. Williams III, 1981: A composite spectrum of vertical shear in the upper ocean. *J. Phys. Oceanogr.*, **11**, 1258–1271, doi:[10.1175/1520-0485\(1981\)011<1258:ACSOVS>2.0.CO;2](https://doi.org/10.1175/1520-0485(1981)011<1258:ACSOVS>2.0.CO;2).
- Gregg, M. C., and E. Kunze, 1991: Internal-wave shear and strain in Santa Monica basin. *J. Geophys. Res.*, **96**, 16 709–16 719, doi:[10.1029/91JC01385](https://doi.org/10.1029/91JC01385).
- Hoskins, B. J., and F. P. Bretherton, 1972: Atmospheric frontogenesis models: Mathematical formulation and solution. *J. Atmos. Sci.*, **29**, 11–37, doi:[10.1175/1520-0469\(1972\)029<0011:AFMMFA>2.0.CO;2](https://doi.org/10.1175/1520-0469(1972)029<0011:AFMMFA>2.0.CO;2).
- Itsweire, E. C., T. R. Osborn, and T. P. Stanton, 1989: Horizontal distribution and characteristics of shear layers in the seasonal thermocline. *J. Phys. Oceanogr.*, **19**, 301–320, doi:[10.1175/1520-0485\(1989\)019<0301:HDACOS>2.0.CO;2](https://doi.org/10.1175/1520-0485(1989)019<0301:HDACOS>2.0.CO;2).
- Jenkins, G. M., and D. G. Watts, 1968: *Spectral Analysis and Its Applications*. Holden-Day, 525 pp.
- Klein, P., B. L. Hua, G. Lapeyre, X. Capet, S. Le Gentil, and H. Sasaki, 2008: Upper-ocean turbulence from high-resolution 3D simulations. *J. Phys. Oceanogr.*, **38**, 1748–1763, doi:[10.1175/2007JPO3773.1](https://doi.org/10.1175/2007JPO3773.1).
- Klymak, J. M., W. Crawford, M. H. Alford, J. A. MacKinnon, and R. Pinkel, 2015: Along-isopycnal variability of spice in the North Pacific. *J. Geophys. Res. Oceans*, doi:[10.1002/2013JC009421](https://doi.org/10.1002/2013JC009421), in press.
- Kunze, E., 1993: Submesoscale dynamics near a seamount. Part II: The partition of energy between internal waves and geostrophy. *J. Phys. Oceanogr.*, **23**, 2589–2601, doi:[10.1175/1520-0485\(1993\)023<2589:SDNASP>2.0.CO;2](https://doi.org/10.1175/1520-0485(1993)023<2589:SDNASP>2.0.CO;2).
- , and T. B. Sanford, 1993: Submesoscale dynamics near a seamount. Part I: Measurements of Ertel vorticity. *J. Phys. Oceanogr.*, **23**, 2567–2588, doi:[10.1175/1520-0485\(1993\)023<2567:SDNASP>2.0.CO;2](https://doi.org/10.1175/1520-0485(1993)023<2567:SDNASP>2.0.CO;2).
- , E. Firing, J. M. Hummon, T. K. Chereskin, and A. M. Thurnherr, 2006: Global abyssal mixing inferred from lowered ADCP shear and CTD strain profiles. *J. Phys. Oceanogr.*, **36**, 1553–1576, doi:[10.1175/JPO2926.1](https://doi.org/10.1175/JPO2926.1).
- Lumpkin, R., and S. Elipot, 2010: Surface drifter pair spreading in the North Atlantic. *J. Geophys. Res.*, **115**, C12017, doi:[10.1029/2010JC006338](https://doi.org/10.1029/2010JC006338).
- Mahadevan, A., 2006: Modeling vertical motion at ocean fronts: Are nonhydrostatic effects relevant at submesoscales? *Ocean Modell.*, **14**, 222–240, doi:[10.1016/j.ocemod.2006.05.005](https://doi.org/10.1016/j.ocemod.2006.05.005).
- Marmorino, G. O., J. P. Dugan, and T. E. Evans, 1986: Horizontal variability in the vicinity of a Sargasso Sea front. *J. Phys. Oceanogr.*, **16**, 967–980, doi:[10.1175/1520-0485\(1986\)016<0967:HVOMIT>2.0.CO;2](https://doi.org/10.1175/1520-0485(1986)016<0967:HVOMIT>2.0.CO;2).
- , L. J. Rosenblum, and C. L. Trump, 1987: Finescale temperature variability: The influence of near-inertial waves. *J. Geophys. Res.*, **92**, 13 049–13 062, doi:[10.1029/JC092iC12p13049](https://doi.org/10.1029/JC092iC12p13049).
- Molemaker, J. J., J. C. McWilliams, and X. Capet, 2010: Balanced and unbalanced routes to dissipation in an equilibrated Eady flow. *J. Fluid Mech.*, **654**, 35–63, doi:[10.1017/S0022112009993272](https://doi.org/10.1017/S0022112009993272).
- Müller, P., R.-C. Lien, and R. Williams, 1988: Estimates of potential vorticity at small scales in the ocean. *J. Phys. Oceanogr.*, **18**, 401–416, doi:[10.1175/1520-0485\(1988\)018<0401:EOPVAS>2.0.CO;2](https://doi.org/10.1175/1520-0485(1988)018<0401:EOPVAS>2.0.CO;2).
- Munk, W., 1981: Internal waves and small-scale processes. *Evolution of Physical Oceanography*, B. A. Warren and C. A. Wunsch, Eds., MIT Press, 623 pp.
- Okubo, A., 1971: Oceanic diffusion diagrams. *Deep-Sea Res. Oceanogr. Abstr.*, **18**, 789–802, doi:[10.1016/0011-7471\(71\)90046-5](https://doi.org/10.1016/0011-7471(71)90046-5).
- Pelland, N. A., C. C. Eriksen, and C. M. Lee, 2013: Sub-thermohaline eddies over the Washington continental slope as observed by seaglidors, 2003–09. *J. Phys. Oceanogr.*, **43**, 2025–2053, doi:[10.1175/JPO-D-12-086.1](https://doi.org/10.1175/JPO-D-12-086.1).
- Poje, A. C., and Coauthors, 2014: Submesoscale dispersion in the vicinity of the Deepwater Horizon spill. *Proc. Natl. Acad. Sci. USA*, **111**, 12 693–12 698, doi:[10.1073/pnas.1402452111](https://doi.org/10.1073/pnas.1402452111).
- Polzin, K. L., E. Kunze, J. M. Toole, and R. W. Schmitt, 2003: The partition of finescale energy into internal waves and geostrophic motions. *J. Phys. Oceanogr.*, **33**, 234–248, doi:[10.1175/1520-0485\(2003\)033<0234:TPOFEI>2.0.CO;2](https://doi.org/10.1175/1520-0485(2003)033<0234:TPOFEI>2.0.CO;2).
- Scott, R. K., 2006: Local and nonlocal advection of a passive tracer. *Phys. Fluids*, **18**, 116601, doi:[10.1063/1.2375020](https://doi.org/10.1063/1.2375020).
- Shcherbina, A. Y., and Coauthors, 2015: The LatMix summer campaign: Submesoscale stirring in the upper ocean. *Bull. Amer. Meteor. Soc.*, doi:[10.1175/BAMS-D-14-00015.1](https://doi.org/10.1175/BAMS-D-14-00015.1), in press.
- Smith, K. S., and R. Ferrari, 2009: The production and dissipation of compensated thermohaline variance by mesoscale stirring. *J. Phys. Oceanogr.*, **39**, 2477–2501, doi:[10.1175/2009JPO4103.1](https://doi.org/10.1175/2009JPO4103.1).
- , G. Boccaletti, C. C. Henning, I. Marinov, C. Y. Tam, I. M. Held, and G. K. Vallis, 2002: Turbulent diffusion in the geostrophic inverse cascade. *J. Fluid Mech.*, **469**, 13–48, doi:[10.1017/S0022112002001763](https://doi.org/10.1017/S0022112002001763).
- Spall, M. A., 1995: Frontogenesis, subduction, and cross-frontal exchange at upper-ocean fronts. *J. Geophys. Res.*, **100**, 2543–2557, doi:[10.1029/94JC02860](https://doi.org/10.1029/94JC02860).
- Stern, M. E., 1975: *Ocean Circulation Physics*. Academic Press, 246 pp.
- Todd, R. E., D. L. Rudnick, M. R. Mazloff, B. D. Cornuelle, and R. E. Davis, 2012: Thermohaline structure in the California Current System: Observations and modeling of spice variance. *J. Geophys. Res.*, **117**, C02008, doi:[10.1029/2011JC007589](https://doi.org/10.1029/2011JC007589).
- Tulloch, R., J. Marshall, C. Hill, and K. S. Smith, 2011: Scales, growth rates and spectral fluxes of baroclinic instability in the ocean. *J. Phys. Oceanogr.*, **41**, 1057–1076, doi:[10.1175/2011JPO4404.1](https://doi.org/10.1175/2011JPO4404.1).
- Veronis, G., 1972: On properties of seawater defined by temperature, salinity and pressure. *J. Mar. Res.*, **30**, 227–255.